

Irreversibility and symmetry breaking in the creation and annihilation of defects in active living matter

A. Be'er,^{1,2} E.D. Neimand,³ D. Corbett,⁴ D.J.G. Pearce,⁴ G. Ariel,⁵ and V. Yashunsky³

¹*Zuckerberg Institute for Water Research, The Jacob Blaustein Institutes for Desert Research, Ben-Gurion University of the Negev, Sede Boqer Campus, Midreshet Ben-Gurion, Israel*

²*The Department of Physics, Ben-Gurion University of the Negev, Beer-Sheva, Israel*

³*The Swiss Institute for Dryland Environmental and Energy Research,*

The Jacob Blaustein Institutes for Desert Research,

Ben-Gurion University of the Negev, Sede Boqer Campus, Midreshet Ben-Gurion, Israel

⁴*Department of Theoretical Physics, University of Geneva, Geneva, Switzerland*

⁵*Department of Mathematics, Bar-Ilan University, Ramat-Gan, Israel*

(Dated: August 22, 2025)

Active living matter continuously creates and annihilates topological defects in a process that remains poorly understood. Here, we investigate these dynamics in two distinct active living systems—swarming bacteria and human bronchial epithelial cells. Despite their entirely different evolutionary origins, biological functions, and physical scales, both systems exhibit half-integer defects, consistent with the nematic phase. However, in contrast to active nematic theory, we find that defect creation and annihilation undergoes spatial symmetry breaking. We propose that this results from a fundamental dualism between nematic structural organization and generated polar forces, which are intrinsic to living systems. Furthermore, our estimation of entropy production reveals that creation and annihilation are not reversed processes. Our findings challenge conventional nematic models and emphasize the role of defect-mediated dynamics in non-equilibrium biological systems as a major source of entropy production.

I. INTRODUCTION

Active nematic materials are typically comprised of elongated components that generate stress at the microscopic scale, leading to large-scale motion [1–4]. Unlike passive systems, active matter remains in a state of perpetual motion and reorganization, which is driven by internally generated forces [5, 6]. A hallmark of active nematic materials is the continuous creation and annihilation of topological defects [7], which result from a balance between active and elastic forces [8–11]. Of particular interest are living systems, such as bacterial collectives [12–16] and tissue cells [17–19], because their physical properties are also related to their biological functions [20–22]. In living matter, active stress originates from metabolism and the consumption of chemical fuel, which enables bacteria and cells to move and generate forces on their neighbors. Elasticity arises from an elongated cellular shape, leading to liquid-crystal-like properties [20–22]. The resulting defects are mesoscopic objects involving tens to hundreds of cells and governed by intrinsic spatiotemporal scales that are independent of system size [12–19].

Experiments with bacterial colonies and cell monolayers consistently reveal half-integer defects, in accordance with nematic symmetry [12–19, 23–25]. Recent studies suggested that nematic symmetry can also manifest in systems with directionality [26], such as models of self-propelled rods [27, 28] and bacterial experiments [29]. Intriguingly, some nematically ordered systems display polar characteristics under specific conditions, indicating the coexistence of nematic and polar symmetries [30–34]. This interplay of symmetries is fundamental to understanding biological processes, such as biofilm formation

and the organization of cellular tissues, yet remains underexplored experimentally.

Defect interactions have been primarily investigated through numerical simulations [35–39]. Elastic forces between defects predict Coulomb-like interactions, as well as additional forces and torques that rely on their relative orientation [40–43]. It has been suggested that nematic active stresses also lead to the generation of hydrodynamic flows around the defects which results in self-propulsion of $+^{1/2}$ defects. Rotational diffusion can reduce persistence in $+^{1/2}$ defect motion, preventing unbinding from $-^{1/2}$ counterparts, and affecting defect density in steady states [36]. However, much of the theoretical framework remains experimentally unverified.

Recent experiments on microtubule-based active nematics and swarming bacteria have uncovered a broad spectrum of defect organization, ranging from giant number fluctuations to hyperuniformity [13, 39, 44]. In fibrosarcoma cell cultures, $+^{1/2}$ defects align toward the edge of the colony, generating chiral edge flows through local chiral active stress [45]. Spontaneous mirror (chiral) symmetry breaking has been demonstrated for $+^{1/2}$ defects, which specifically concentrate at the boundary between vorticity-dominated and strain-rate-dominated regions in microtubule-kinesin films, highlighting their strong coupling to large-scale hydrodynamic fluxes within the material [29]. However, the creation and annihilation processes, which we identified below as primary sources of energy injection and dissipation in living systems, are underexplored and necessitating experimental validation of current theoretical predictions.

In this paper, we experimentally study swarming bacteria [20] and human bronchial epithelial cells (HBECs)

[19]—distinct systems that both display nematic half-integer defects. Our findings reveal that the creation and annihilation of defects follow distinct, previously unrecognized trajectories that spontaneously break mirror symmetry—a feature absent in standard active nematic models. We also find that these trajectories exhibit time-reversal symmetry breaking, a hallmark of non-equilibrium processes. Statistical analysis reveals that defect creation and annihilation drive substantial entropy production, underscoring their irreversible nature and critical role in active matter organization. Finally, we demonstrate why these observations can be explained by taking into account directional (polar) self-propulsion in bacteria and cells.

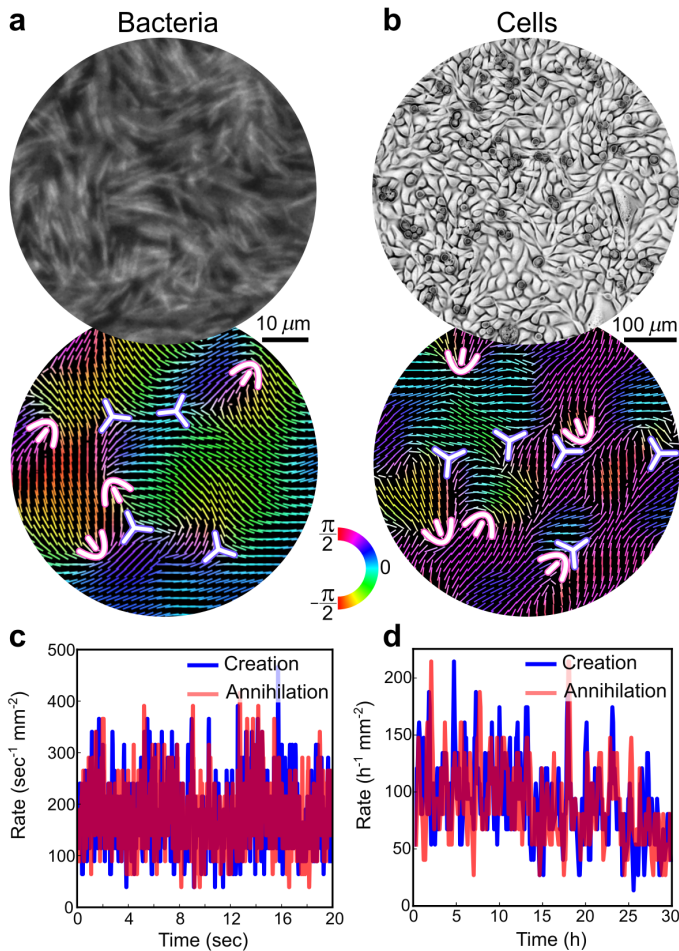


FIG. 1: Director field and nematic defects in swarming *Bacillus subtilis* and human bronchial epithelial cells (HBECs) monolayers. The nematic director field, colored according to the orientations (ranging from $-\pi/2$ to $\pi/2$), and half-integer defects in (a) swarming *B. subtilis* and (b) HBECs. $+^{1/2}$ types are represented as pink comet shapes and $-^{1/2}$ as violet tripods. (c, d) Rates of pair-creation (blue) and annihilation (red) of oppositely charged $\pm^{1/2}$ defects; (c) swarming *B. subtilis* and (d) HBECs.

II. RESULTS

Half-integer defects in bacteria and cells

We study the creation and annihilation of defects in two highly active, quasi-turbulent living systems of swarming *Bacillus subtilis* bacteria [13] and human bronchial epithelial cells (HBECs) [19]. Despite the extreme disparity in the time scales and dimension (Fig. 1), both systems share fundamental characteristics of active extensile nematics [8, 46]: (i) A steady-state mixture of half-integer defects (Figs. 1a-b), which is obtained through continuing creation and annihilation events (Figs. 1c-d), (ii) a counter-rotating vortex pattern around defects with (iii) an exponential distribution of vortex sizes [19, 45].

The defects are created and annihilated in pairs with opposite charges. In both systems, the rates of creation and annihilation events fluctuate over time but stabilize to a steady state (Figs. 1c-d), implying an approximately constant number of defects over time with a total charge that fluctuates around zero. We characterize the motion of defect pairs through these observables, see the sketch in Fig. 2.

- t : time from creation or annihilation event (negative time indicates time before annihilation).
- d : the distance between the $+^{1/2}$ and $-^{1/2}$ defects in the pair.
- γ : the argument of the vector from the $-^{1/2}$ to the $+^{1/2}$ defect core, rotated so that $\gamma(t = 0) = 0$.
- φ^+ : the angle between the orientation of the “tail” of the comet-shaped $+^{1/2}$ defect and the vector connecting the pair. Thus, $\varphi^+ = 0$ indicates that the tail is pointing away from the $-^{1/2}$ defect.
- φ^- : the angle between the orientation of one of the $-^{1/2}$ legs and the line connecting the pair. We use the smallest angle out of the three legs. For example, $\varphi^- = 0$ implies that one of the legs is pointing towards the $+^{1/2}$ defect.
- $\delta = \varphi^+ - 3\varphi^- - \pi$: pair orientation offset. This gives a measure of how compatible the orientations of the defects are with each other. $\delta = 0$ suggests the defects are at the orientations that minimize the variation in the nematic field between them[41].

Spontaneous breaking of the mirror symmetry in defect orientation

At annihilation or creation events, defect pairs are in phase ($\delta = 0$; see Figs. 2a-b), indicating they are perfectly aligned. When $\delta \neq 0$, the elastic energy between

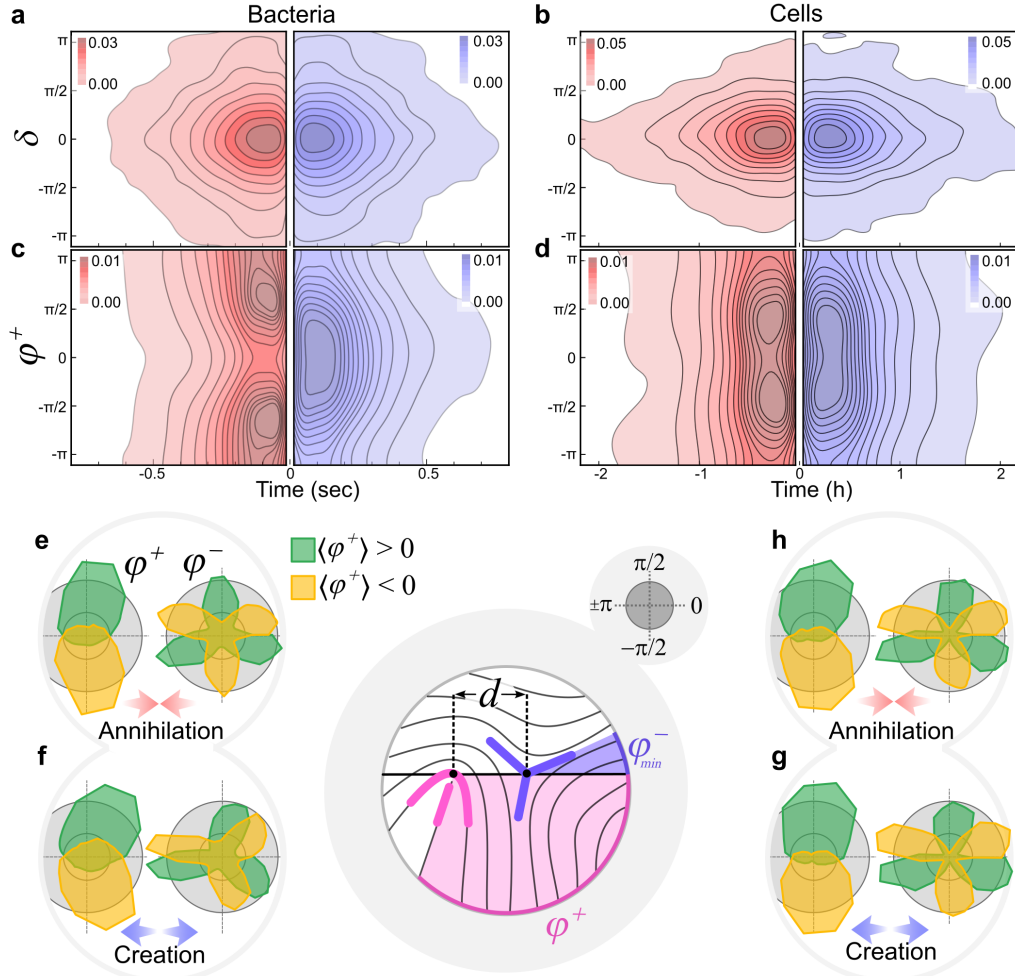


FIG. 2: Configuration of $+^{1/2}$ and $-^{1/2}$ defect-pairs during creation and annihilation. Sketch: Definitions of orientational angles φ^+ (pink) and φ^- (violet) for paired $+^{1/2}$ and $-^{1/2}$ defects relative to the pair axis connecting between $+^{1/2}$ and $-^{1/2}$ defect centers (horizontal black line). **(a, b)** Distribution of the pair orientation offset angle, $\delta = \varphi^+ - 3\varphi^- - \pi$, as a function of time for creation (blue) and annihilation (red) events. $\delta = 0$ implies that the nematic director fields of the paired-defects are synchronized. **(c, d)** Distribution of φ^+ as a function of time for the creation (blue) and annihilation (red) events. The creation/annihilation instant is indicated by $t = 0$, with negative time indicating time to annihilation, and positive time is from creation. Red and blue color intensities indicate probability density. **(e-g)** Alignment of defect pairs, classified by the mean orientation of the $+^{1/2}$ defect during its trajectory, $\langle\varphi^+\rangle$. Angular distributions of $\varphi^+(d < r_0)$ and $\varphi^-(d < r_0)$ within $r_0 = 15 \mu\text{m}$ for bacteria and $35 \mu\text{m}$ for cells are shown for “up” ($\langle\varphi^+\rangle > 0$, green) and “down” ($\langle\varphi^+\rangle < 0$, yellow) configurations in bacteria (e, f) and cells (g, h).

the defects diverges at small separations, indicating that the defects align at very short distances [41].

We next look at the alignment of the $+^{1/2}$ defect with the line connecting the defects in the pair, captured by the parameter φ^+ . We see a bimodal distribution for φ^+ immediately before annihilation with peaks at $\pm\pi/2$; see Figs. 2c-d. This indicates that the tail of the positive defect is perpendicular to the direction of annihilation at the end of this process. A similar but less pronounced effect is also visible immediately after creation. This bimodality indicates a spontaneously broken chiral symmetry in the orientation of the defects. To quantify

this effect, we split all trajectories into two groups based on their time-averaged orientation across the full trajectory, either “up” (average $\varphi^+ > 0$) or “down” (average $\varphi^+ < 0$). The orientation φ^- follows a similar symmetry breaking, consistent with $\delta = 0$ (Figs. 2e-f).

Spiraling trajectories of creation and annihilation

The separation rate between paired defects (Figs. 3a-b) is characterized by increased speed close to the creation or annihilation events, consistent with theoretical

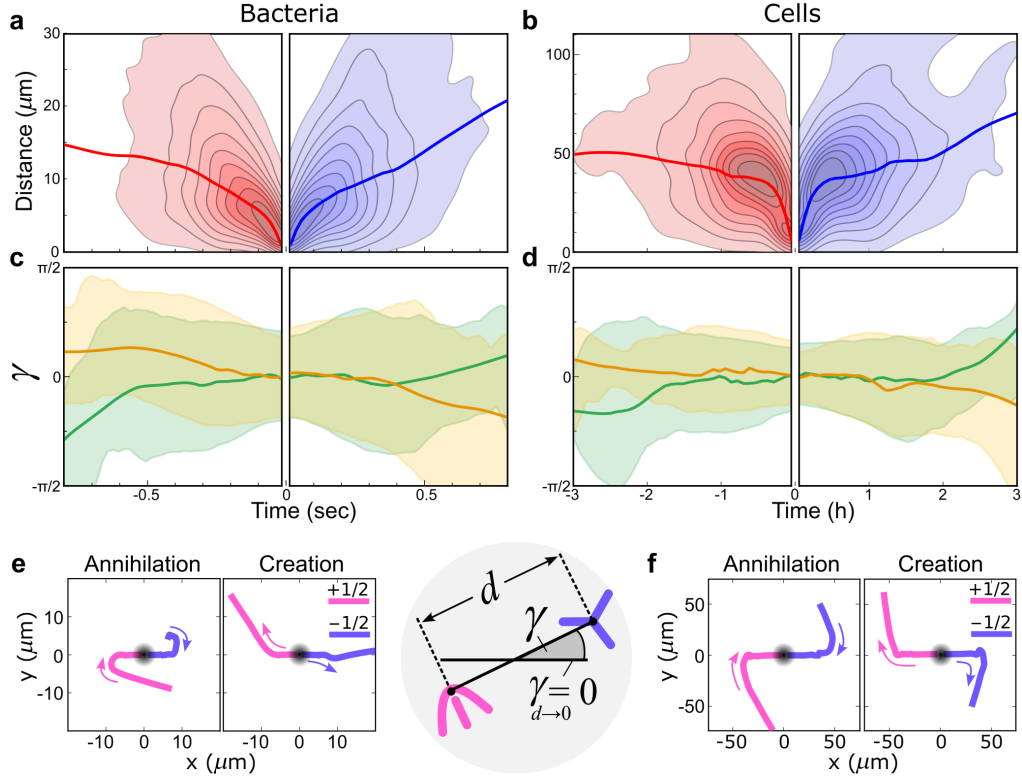


FIG. 3: Spiraling trajectories of creation and annihilation. Sketch: Co-rotation angle γ —the line connecting between the location of defect centers with respect to the angle close to creation/annihilation instant ($\gamma_{d \rightarrow 0}$). (a, b) Distance between $\pm^{1/2}$ defect-pairs as a function of time after creation (blue) and before annihilation (red), for bacteria and cells. The creation/annihilation instant is indicated by $t(d \rightarrow 0)$, with negative values indicating time to annihilation, and positive ones indicating time from creation. Solid lines represent the average trajectories, while red and blue color intensities indicate probability density. (c, d) Time evolution of γ (the angle of the line connecting the defect-pairs, aligned to $\gamma_{d \rightarrow 0} = 0$). Solid lines represent averages for “up” (green) and “down” (yellow) configurations. Shaded areas indicate the standard deviation. (e, f) Average trajectories of $+^{1/2}$ (pink) and $-^{1/2}$ (violet) defects during creation and annihilation, measured in the lab frame of reference. Trajectories are centered around the creation/annihilation position (black point), rotated to $\gamma_{d \rightarrow 0}$ and mirrored to the “up” configuration.

predictions for defect annihilation in passive systems [41]. However, defects do not move in a straight line. This is quantified by the orientation of the vector connecting the defects changes over time, $\gamma(t)$. Generally, γ varies monotonically with time, indicating that defect pairs tend to co-rotate during the process of annihilation or creation. Furthermore, the chirality of the co-rotation is correlated with the “up” or “down” configuration (Figs. 3c-d).

Lastly, Figs. 3e-f show averaged trajectories for creation and annihilation events in the “up” configuration. This reflects the spiraling motion toward (away) each other during annihilation (creation). These trajectories are similar to those predicted for the annihilation of topological defects with an initial phase disparity [41].

Spontaneous breaking of the mirror symmetry in flow fields

We find that flows around defect pairs also exhibit mirror symmetry breaking (Figs. 4a-d, Extended Data Figs. 1-2). Flows were measured separately for the “up” and “down” orientations. In bacteria, the forward flow at the core of the defect $+^{1/2}$ is offset relative to the defect symmetry axis. The direction of the tilt changes between annihilation and creation (Extended Data Fig. 1). In particular, for both bacteria and cells, the flow at the core of the $-^{1/2}$ defects exhibits a distinct rotational behavior, rotating clockwise for “up”-oriented configurations (Fig. 4B, Extended Data Figs. 1b,f and 2b,f) and counterclockwise for “down”-oriented configurations (Fig. 4d, Extended Data Figs. 1d,h and 2d,h). The flows around unpaired defects (Figs. 4e-f) retain mirror symmetry, in agreement with theoretically predicted flows around isolated defects in extensile active nematics.

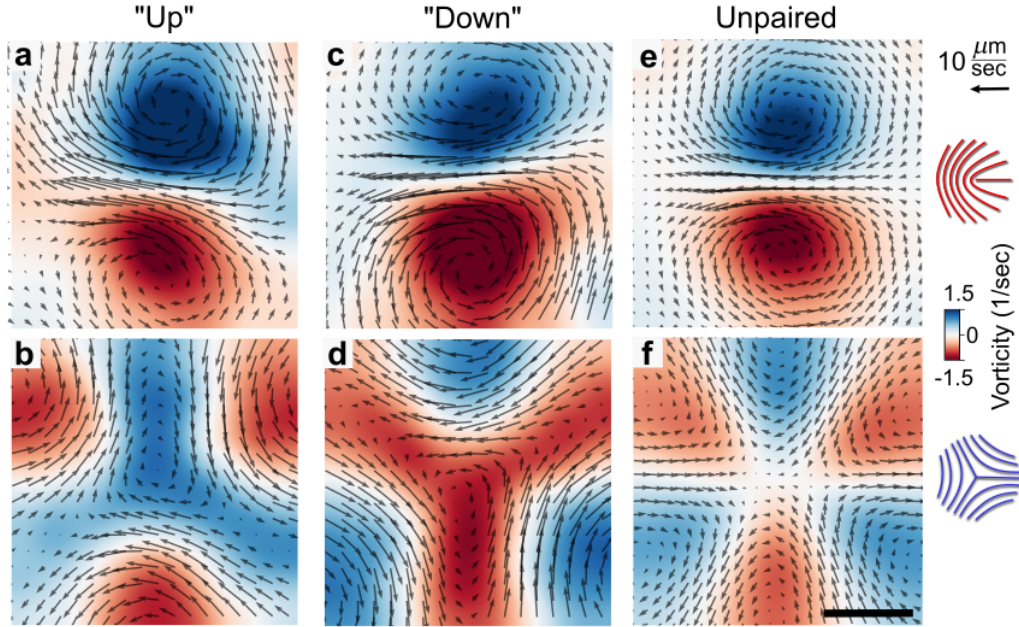


FIG. 4: Ensemble-averaged flow fields near $\pm^{1/2}$ defect pairs. (a, b) Average velocity fields (black arrows) and vorticity distributions (heatmap) around defects. (a-d) Flow fields around paired $+^{1/2}$ and $-^{1/2}$ defects, averaged separately for the “up” (a, b) and “down” (a, d) configurations. e, f) Flow fields around unpaired $+^{1/2}$ and $-^{1/2}$ defects. For clarity, only results for bacteria close to annihilation are shown. The angular orientation of defects is illustrated in the schematic. Arrow and spatial scales are indicated. Scale bar: 10 μm . The number of fields averaged to obtain each panel is: (a) 5459; (b) 5391; (c) 5336; (d) 5323; (e) 89027; (f) 88267.

The source of mirror symmetry breaking

In addition to nematic order, bacteria and cells also exhibit a polar symmetry due to their directed self-propulsion mechanism. Combining nematic interactions with active stresses of various symmetries can significantly alter active nematic behavior [28, 47].

To describe cell self-propulsion, we introduce a polar field, p , indicating the direction of cell movement relative to the substrate, alongside the nematic field that describes the cells’ long axes. This can be visualized as two superimposed parallel fields: one with lines for the long axes and another with arrows for the head direction (see Fig. 5a). For simplicity, we assume that both p and $-p$, the latter pointing in the opposite direction, are compatible with the same nematic field.

During creation in extensile nematics, defects arise from a bend instability that introduces a net curl to the polar field and breaks chiral symmetry (Fig. 5a), with a particularly strong net curl around the $+^{1/2}$ defect (green arrow; Fig. 5a). Notably, the mirror image of this process produces defects with opposite chirality, indicating that defect chirality selection is driven by spontaneous symmetry breaking. In this context, distinct “up” and “down” defect configurations should emerge during creation.

Around an isolated defect, the polar field exhibits a net polarization and curl that depend on the grain boundary

position, see SI for a derivation. This polar field indicates the force direction exerted by neighboring particles, generating both force and torque on the defect core (Fig. 5a). A similar symmetry breaking mechanism has been noted in simulations of self-propelling thin rods and flexible polymers [48–50].

We suggest that defect dynamics and flows around the defects in our experiments result from a combination of torque and extensile active stress. For a $+^{1/2}$ defect, this leads to an offset force along the defect’s symmetry axis and an additional net torque. $-^{1/2}$ defect experiences smaller net torques and forces, allowing for self-propulsion and rotation. The calculated Stokes flow field around isolated defects (Figs. 5c-d) indicates that immediately after the defects are created, flow patterns exhibiting opposite chiral symmetry are equally likely.

This symmetry breaking can explain the distinct behavior of “up” and “down” configurations as follows. Defects are generated through a bend instability induced by extensile active stress, hence are generated with $\varphi^+ \approx 0$. After creation, $+^{1/2}$ move in a curved trajectory, spiraling away from its $-^{1/2}$ pair due to the non-zero curl resulting from the polar field. Figure 5a illustrates a situation where a $+^{1/2}$ defect moves, rotating clockwise. Consequently, this leads to the defect pair to also rotate clockwise, which we refer to as “up” configuration (see Fig. 4).

The polar grain boundary connected to the defect core is topologically constrained and persists throughout the

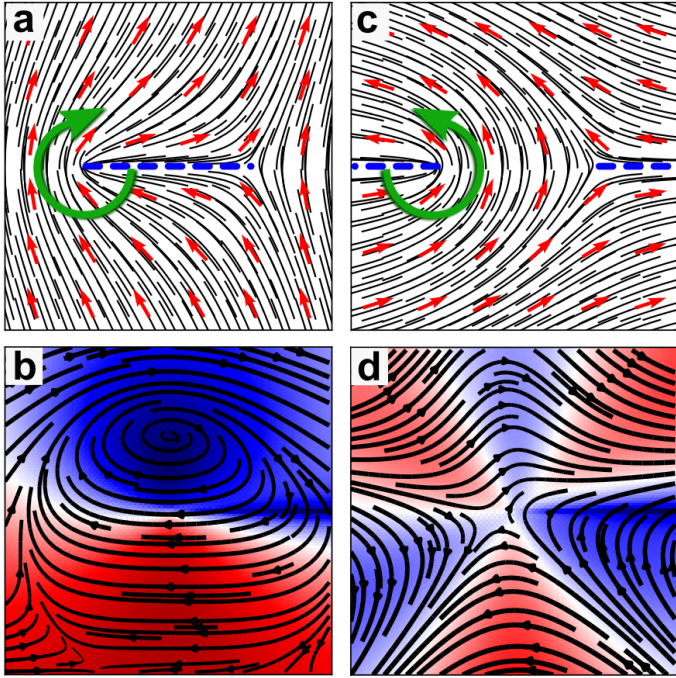


FIG. 5: The interaction between nematic and polar symmetries. (a) Defect creation via bend instability with the overlaid polar field, indicated by red arrows; a grain boundary in the polar field is introduced indicated by the blue dashed line. The polar field leads to a torque on the defects, indicated by the green arrow. The torque will reorient the $+^{1/2}$ defect, causing it to self-propel around the $-^{1/2}$ defect. Shown here is the “up” configuration. (b) Nematic and polar fields around a pair of defects before annihilation. Here the grain boundaries do not directly connect. The same torque is present around the $+^{1/2}$ defect that can lead to a spiral trajectory. (c) & (d) Predicted Stokes flow field around a (c) $+^{1/2}$ and (d) $-^{1/2}$ defect with additional active force along the polar direction; shown in the “up” configuration.

defect’s lifetime. As a result, the same broken symmetry influences the defect annihilation process, as illustrated in Fig. 5b. When a $+^{1/2}$ defect approaches annihilation, two key forces dictate its trajectory. The first is the elastic attraction to the $-^{1/2}$ defect with which it is annihilating, and the second is the active self-propulsion force. The chiral torque acting on the defect causes it to rotate, so it does not self-propel directly toward the $-^{1/2}$ defect; however, the elastic forces prevent complete escape. Consequently, the resulting trajectory forms an inward spiral toward annihilation, as depicted in Figs. 3e-f. In contrast to the creation process, annihilation is independent of φ^+ (assuming $\delta = 0$). Thus, defects can annihilate even when $\varphi^+ \neq 0$, as shown in Figs. 2c-d. Additionally, the reverse of this process is equally likely, resulting in the observed “up” and “down” configurations during annihilation.

Time-reversal symmetry breaking

Active systems are typically irreversible, which is manifested in strictly positive entropy production (EP). Loosely speaking, EP is defined as the Kullback-Leibler divergence (KLD) from the distribution of trajectories compared to the distribution of time-reversed trajectories [51, 52]. In some systems, such as Langevin particles satisfying the Einstein relation, EP equals (in units of temperature) to the dissipated heat [52, 53]. It has been suggested that EP also plays a role in active systems, and is indicative of the amount of extractable work [52, 53]. Previous attempts to quantify EP in bacterial and cellular dynamics proved challenging. In [53], local EP in swimming bacteria was estimated using a compression-based methods, and found positive EP mainly close to walls or barriers. However, negligible or no EP was observed in the bulk, despite the fact that the system is highly active and out of equilibrium.

Obtaining accurate statistics of the joint distribution of cellular or bacterial trajectories is challenging because of the high dimensionality of such a dataset as estimating KLD suffers from severe undersampling of the phase space [53]. Here, defects provide physically motivated coarse-graining of the micro-scale motion into a mesoscopically observable feature. As a consequence, all the estimates reported here are lower bounds to the actual EP.

In extensile-active nematics, $+^{1/2}$ defects move in a direction that is opposite to the “comet-tail” [8]. To quantify this effect, Table III shows the average projection of the defect direction onto the velocity, which is indeed negative. We can calculate a similar measure by contracting the velocity of a $-^{1/2}$ defect with the third rank tensor that describes its orientation (see Methods). Interestingly, we find a non-zero average value (Table III) that is not expected in a typical active nematic. This is consistent with the net force we calculate on the core of a $-^{1/2}$ defect resulting from the polar active forcing (see SI).

Table III also shows results for EP estimates. For bacteria, we find a high value of EP in $+^{1/2}$ defects, and lower (but statistically significant) for $-^{1/2}$ ones. For cells, the EP in $+^{1/2}$ cells is an order of magnitude smaller than for bacteria. For $-^{1/2}$ it is below the error range.

Next, we turn to analyze creation and annihilation events. Figures 2c-d show that the distribution of $+^{1/2}$ is different close to creation compared to annihilation. Similar broken symmetries can also be observed in the average trajectories (Figs. 3e-f) and the flow fields (Extended Data Figs. 1 and 2). To quantify this, Table II details the results for EP estimates. The dimension D indicated the length of the trajectories used (starting at the event). Indeed, our results show positive EP both for bacteria and cells.

Focusing on time-reversal, running the experimental movies backward, creation will appear as annihilation

TABLE I: Entropy production (EP) estimation for isolated defects. The row noted projection shows the projection of the defect orientation on the velocity. The row noted EP shows a statistical estimate for a lower bound for the entropy production rate obtained for defect trajectories. Values show the estimate \pm the standard error. Since this is a lower bound, a value that is statistically larger than zero implies non reversible dynamics. See the methods section for details.

Defect charge	Bacteria		Cells	
	$+^{1/2}$	$-^{1/2}$	$+^{1/2}$	$-^{1/2}$
projection	-0.2 ± 0.003	0.005 ± 0.003	-0.08 ± 0.003	0.01 ± 0.003
EP	0.94 ± 0.03	0.005 ± 0.003	0.18 ± 0.01	0.0006 ± 0.0007

TABLE II: Entropy production (EP) estimation for defect pairs. The table shows different statistical estimates for a lower bound for the entropy production rate obtained for defect trajectories. The dimension D indicated the length of the trajectories used (starting at the event). Values show the estimate \pm the standard error. Since this is a lower bound, a value that is statistically larger than zero implies non reversible dynamics. See the methods section for details.

*Note that the KLD is a non-negative quantity. However, the estimator are random variable with an error that is normally distributed with the noted standard deviation. Hence, zero EP my result in a negative estimate that is several times the standard error. In statistical terms, the hypothesis that $EP = 0$ cannot be negated.

Event	Bacteria			Cells		
	creation	annihilation	cross	creation	annihilation	cross
$EP(D = 2)$	0.075 ± 0.008	0.04 ± 0.008	$-0.01 \pm 0.005^*$	0.63 ± 0.03	0.55 ± 0.03	0.4 ± 0.3
$EP(D = 5)$	0.11 ± 0.01	0.14 ± 0.02	0.06 ± 0.02	0.46 ± 0.04	0.47 ± 0.05	$-0.04 \pm 0.03^*$

and vice versa. To this end, Table II shows the cross entropy between forward-creation/backward-annihilation and forward-annihilation/backward-creation. The dimension D indicated the length of the trajectories used (starting at the event). The positive cross-entropy indicated that creation and annihilation are not time-symmetric, both for bacteria and cells.

Comparing the total EP rates, we need to consider the rate of creation and annihilation events. For bacteria, the time between events is about 1 sec (50 frames), hence the total EP due to movement is about 50 times larger than due creation-annihilation. For cells, the time between creation and annihilation is about 2 hrs (24 frames). Hence, EP due to movement is comparable to EP due to creation-annihilation. These differences are consistent with the observation that in bacteria, $\pm^{1/2}$ defects appear self-propelled in the sense that their trajectories are ballistic over short time periods [13], implying a relatively large EP. With cells, both $\pm^{1/2}$ defects are diffusive [19], their movement in the bulk is close to reversible, and EP is most apparent in creation and annihilation.

Conclusions

Living systems constantly produce and consume energy, keeping them far from thermodynamic equilibrium. This continuous energy input drives self-organization, often breaking spatial symmetries in ways that shape the biological function [47, 54, 55]. A compelling hypothesis suggests that living systems leverage topological mecha-

nisms to regulate their organization, providing a unifying framework for understanding emergent behaviors across biological systems [40, 56].

Here, we explore this idea in two seemingly different systems: *Bacillus subtilis* bacterial swarms and human bronchial epithelial cells. Despite stark differences in biological function and physical properties, both systems exhibit active nematic organization, in which rod-shaped bacteria and elongated polygonal cells align and form dynamic topological defects. While bacteria propel in a thin fluid layer at low Reynolds numbers ($\sim 10^{-4}$) [20, 21], HBECs move via substrate adhesion and traction forces. In both cases, motion is highly dissipative and sustained only through continuous energy consumption at the cellular level [57]. Both systems reveal nematic order, where $\pm^{1/2}$ defects undergo continuing creation and annihilation events between defects pairs with opposite charge.

The non-equilibrium and irreversible nature of active living systems is unequivocal. Because bacteria and cells are self propelled, the dynamics is out of equilibrium even at the level of the individual. Therefore, the theoretical prediction is that irreversibility should be observed at the single-cell level. However, the difficulty in capturing irreversibility from individual positions and orientations is reasonable. For any observed single-cell trajectory, one can imagine a cell following the reversed path. Thus, EP from single cells is only expected to be captured by adding intra-cellular degrees of freedom corresponding to chemical and biological function, or possibly also the underlying self-propulsion mechanism.

We can think of defects as physically intuitive, virtual

meso-scpic degrees of freedom. Virtual in the sense that they are not the particles of which the system is made of. Meso-scpic since each one is defined by a small local collective on several close cells. Our findings show that irreversibility is statistically evident locally at the level of the collective. Moreover, we find that defect creation and annihilation are not reciprocal processes that general entropy. This is also physically intuitive as continuous creation of defects in nematic systems is a hallmark of activity. In both experimental systems, entropy production during defect creation and annihilation accounts for a disproportionately large fraction of total entropy production. In cells, it is an order of magnitude higher, suggesting that these events are key drivers of non-equilibrium dynamics rather than incidental fluctuations. Still, one should remember that our estimates are merely lower bounds for the actual EP, which means that quantitative comparison is problematic.

We find that mirror symmetry, predicted by linear nematodynamic theory, spontaneously break in the process of creation and annihilation. Specifically, when close to each other, $+1/2$ spontaneously align perpendicularly (“up” or “down”) to the pair axis (Fig. 2 e-g). Each of these configurations follows spiral-like trajectories rotating either in the clockwise (“up”) or counterclockwise (“down”) direction (Fig. 3 c-f), further indicating spontaneous breaking of the mirror symmetry.

We propose that directional self-propulsion disrupts the nematic symmetry that otherwise captures the coarse-grained behavior of bacterial swarms and epithelial cell monolayers.

This reinforces the role of topological defects in understanding principles of self-organization in living systems.

Our results challenge the standard active nematic description often applied to active living matter. By uncovering these universal physical principles, we take a step toward a deeper understanding of biological self-organization, revealing the fundamental role of symmetry in shaping life at multiple scales.

III. METHODS

Swarming bacteria

Experiments were conducted on *Bacillus subtilis* 3610, the “wild-type” (WT) strain, which is a rod-shaped flagellated species with dimensions $1 \mu\text{m} \times 7 \mu\text{m}$. Cells are stored at -80°C in frozen stocks. Fluorescently labeled variants, green and red, are used (*amyE::PvegR0_sfGFP;specR* and *amyE::Pveg_R0_mKate;specR*); labeling does not affect any known measured quantity. In order to resolve the cells in the crowded colony, we mix the two labeled strains at ratio 1 : 1 (after separate overnight growth), which yields much sparser fields of view (see camera settings next). Swarm experiments are typically done in a standard Petri-dish (8.8 cm in diameter), where the colonies are grown on soft agar (0.5 % and 25 g/L LB) and aged in ambient lab conditions (24°C and 35 % RH) for 4 days. The latter forms the thicker colony structure compared to results obtained in other past studies. Overnight cultures are grown from isolated colonies (which are grown from frozen stocks on hard agar plates (2 % and LB)) at shaking (200 rpm and 30°C) for 18 h in LB liquid medium (2 mL in a 15 mL tube). A small drop of overnight culture (4 μL), either from a single strain, or a 1 : 1 mix of the two labeled variants, is deposited on the agar in the middle of the plate. The colonies grow for a few hours in a 95 % RH incubator at 30°C . The swarm colonies form a quasi-2D structure with a thickness of $\sim 7 \mu\text{m}$, which is uniform along centimeter-wide distances. Observations are done using an optical microscope (Axio Imager Z2 Zeiss; 40 \times) operated at fluorescence mode; this magnification yields a $150 \mu\text{m} \times 150 \mu\text{m}$ observation frame. The system is equipped with a splitting device (Optosplit II) that enables dual excitation and acquisition. The two fluorescence fields are obtained for the same spatial field and time. The image is projected on a NEO camera with 1800×900 pixels and at 50 frames per second so that the green cells are seen on the left panel while the red ones are seen on the right panel. In the current study we focus on the upper layer of the colony. The system operates with the dual fluorescence set Ex 59026x, beam splitter 69008bs, and Em 535/30; 632/60. A compensation lens (an integral part of the Optosplit II device) is used to adjust the focus in each of the panels so that both the green panel and the red one are in focus at the upper layer.

Human bronchial epithelial cells (HBECs)

Human bronchial epithelial cells (HBECs) cultured as previously reported. HBEC culture was executed in a supplemented keratinocyte serum-free medium with l-glutamine (Keratinocyte-SFM with l-glutamine; Gibco). Cells were maintained at 37°C under 5 % CO_2 partial

pressure and 95 % relative humidity. For time-lapse experiments, cells were seeded at a density of approximately 640,000 cells per well in polystyrene (TPP) 12-well tissue culture plates. Time-lapse microscopy experiments were performed in phase contrast on an automated IX71 inverted microscope (Olympus) equipped with the same temperature, humidity, and CO_2 regulations as in culture (Life Imaging Services). Images were acquired using a 10 \times objective, providing a 1.5 mm \times 1.5 mm observation frame. The intervals between images were set to 5 minutes.

Measurement of Velocity and Director Fields

Image analysis was conducted using custom Python code. To obtain the velocity field from microscopic images, we employed the Gunnar Farneback method available from OpenCV library producing displacement vectors for every pixel rather than a sparse set of points. The director field was computed using the second-moment matrix, implemented with the structure tensor function from the skimage Python library. Both the flow and director fields were computed with an averaging window size of 2.5 $\mu m \times$ 2.5 μm for bacteria and 11.1 $\mu m \times$ 11.1 μm for cells.

Defect Detection and Tracking

Nematic defects were identified using the winding number method, which quantifies the degree of rotation in the nematic field around any closed loop of nearest neighbors. When the loop encircles a defect, the winding number reflects the charge of that defect. The orientation of the defects was calculated following the method outlined by Vromans & Giomi (2016) [43]. Angles are discrete, at integer multiples of $\pi/50$. Defect trajectories were automatically tracked using the TrackMate plugin in ImageJ software, which was combined with defect orientation data. This generated a list of defects along with their charges, angles, and locations.

Overall, the data on a single $+^{1/2}$ defect trajectory is a sequence of vectors $\mathbf{p}_0, \dots, \mathbf{p}_K$, where each vector \mathbf{p}_i is in R^3 , i.e., each frame consists of 3 scalar values, corresponding to the $x - y$ coordinates and an angle, corresponding to the orientation of the $+^{1/2}$ defect. The data on a single $-^{1/2}$ defect trajectory is a sequence of vectors $\mathbf{n}_0, \dots, \mathbf{n}_K$, where each vector \mathbf{n}_i is in R^5 , i.e., each frame consists of 5 scalar values, corresponding to the x-y coordinates and the three angles, corresponding to the three directions of the $-^{1/2}$ defect. They may not be exactly $2\pi/3$ apart. Velocities were taken as the displacements between consecutive frames with no further smoothing.

Defect-Pair Detection

To identify defect-pairs, thresholds for distance (Δd) and time (Δt) were applied. The thresholds were set at $\Delta d = 2 \mu m$ for bacteria and $\Delta d = 11.1 \mu m$ for cells, with $\Delta t = 0.04$ seconds for bacteria and 10 minutes for cells. Two oppositely charged defects, $a(t_a, x_a, y_a)$ and $b(t_b, x_b, y_b)$ were considered a created pair if their initial detection times, t_a and t_b , satisfied $|t_a - t_b| < \Delta t$, and their initial locations, x_a, y_a and x_b, y_b , satisfied $((x_a - x_b)^2 + (y_a - y_b)^2)^{1/2} < \Delta d$. Similarly, oppositely charged defects were identified as annihilation pairs if their final detection times and locations met the same criteria. The pair detection algorithm is designed to prevent more than one annihilation or creation event for any defect. Each defect's trajectory is assigned a unique identifier, ensuring that the same identifier cannot be used in more than one pair. Trajectories that span fewer than five consecutive frames were excluded from the analysis. Events near the edge of the frame were excluded to prevent interference from off-frame defects. Additionally, defects appearing at the start or disappearing at the end of the time sequence were not considered created or annihilated to ensure accuracy. The detection algorithm identified 1679 creation and 1676 annihilation events in bacteria from three experimental replicas, and 1201 creation and 1187 annihilation events in HEBCs from six experimental replicas.

Overall, the data on a single defect-pair is a sequence of vectors $\mathbf{x}_0, \dots, \mathbf{x}_K$, where each vector \mathbf{x}_i is in R^8 (x, y coordinates of each defect, one angle for $+^{1/2}$ and three angles for $-^{1/2}$). For a creation event, \mathbf{x}_0 is the measurement closest to creation. For an annihilation event, \mathbf{x}_K is the measurement closest to annihilation. Furthermore, each pair-trajectory is classified as either “up” or “down”, based on the average projection of the $+^{1/2}$ direction on the direction connecting the pair (see sketch, Fig. 2). Specifically $\langle \varphi^+ \rangle > 0$ was defined as “up” and $\langle \varphi^+ \rangle < 0$ as “down”, where $\langle \cdot \rangle$ denotes the circular mean over the trajectory of the paired $+^{1/2}$ defect.

Trajectories of Creation and Annihilation

To describe the average trajectory of creation and annihilation events, consider the k 'th trajectory with defined positions. The distance between defect-pairs is calculated as the Euclidean distance between the defect centers, $d = ((x_a - x_b)^2 + (y_a - y_b)^2)^{1/2}$, where a and b refer to the $+^{1/2}$ and $-^{1/2}$ defects, respectively. The angle of each defect, $\theta_{a/b}(t)$, was measured at various points along its trajectory relative to the position of the creation/annihilation event (x_0, y_0). Since “up” and “down” defects rotate in opposite directions, we analyzed and averaged the trajectories of the “up” and “down” configurations separately. Finally, we combined the “up” and “down” trajectories by transforming the averaged “down” trajectory $\langle \theta_{a/b}(t) \rangle$ into $\langle -\theta_{a/b}(t) \rangle$.

Average Director and Flow Fields Around Defects

To measure the average fields around $\pm^{1/2}$ defects, we analyzed all defect-pairs based on their configuration (“up” or “down”) and trajectory type (“creation” or “annihilation”), resulting in four distinct groups. Defects were analyzed alongside their corresponding flow fields within a window of $35 \mu\text{m} \times 35 \mu\text{m}$ for bacteria and $300 \mu\text{m} \times 300 \mu\text{m}$ for cells, centered at the defect core. The local director and velocity fields were then rotated to align all defects in the same orientation. Finally, the averaged, aligned fields were calculated for each defect type and group.

Quantifying irreversibility in single-defect trajectories

Here, we provide details for the statistical estimates presented in table III.

For each $+^{1/2}$ defect, the detection algorithm described above provides a sequences of positions in 2D and orientation angle, $\theta \in [0, 2\pi)$. The defect velocity v is obtained from the displacements between consecutive frames (next frame - current frame). Denoting the velocity direction $\hat{V} = v/|v|$ and vectorial orientation $\hat{n} = (\cos \theta, \sin \theta)$, the projection of the defect orientation on the velocity direction (row 1 in table III) is $\hat{V} \cdot \hat{n}$. The table shows the mean over all defects \pm the standard error.

For each $-^{1/2}$ defect, the detection algorithm described above provides a sequences of positions in 2D and three orientation angles, corresponding to the directions of the three legs $\theta_1, \theta_2, \theta_3 \in [0, 2\pi)$. We define the average defect direction (taking into account the rank three tensor symmetry) as $p = \sum_i (\cos \theta_i, \sin \theta_i)$. The angle corresponding to the defect orientation is then $\varphi = \tan^{-1}(p_y/p_x)/3$. Note that a function such as atan2 should be used to obtain an angle in $[0, 2\pi)$. Finally, the projection of defect orientation in the velocity direction (angle ψ) is given by $\cos 3(\varphi - \psi)$. The table shows the mean over all defects \pm the standard error.

To estimate EP, forward trajectories use the same single-frame projections described above. For backward trajectories, each trajectory is reversed and analyzed similarly. Note that this changes the sign of velocities and also the corresponding angle φ for which it is associated (because velocities are a forward difference rule). For example, to obtain $+1/2$ trajectories of length d , we look at frame segments of length $d + 1$. The data for such a segment consists of $(x_1, y_1, \theta_1), \dots, (x_{d+1}, y_{d+1}, \theta_{d+1})$, where (x, y) are the center of mass positions and θ the defect orientation. The forward velocities are $v_i^F = (x_{i+1} - x_i, y_{i+1} - y_i)$, and the forward orientations, $\hat{p}_i^F = (\cos \theta_i, \sin \theta_i)$, $i = 1 \dots d$. Then, the forward projections trajectory is $\vec{F} = (\hat{v}_1^F \cdot \hat{p}_1^F, \dots, \hat{v}_d^F \cdot \hat{p}_d^F)$, with $\hat{v}_i^F = v_i^F / \|v_i^F\|$. Similarly, the backward trajectory is $\vec{B} = (\hat{v}_1^B \cdot \hat{p}_1^B, \dots, \hat{v}_d^B \cdot \hat{p}_d^B)$, with $v_i^B = (x_i - x_{i+1}, y_i - y_{i+1}) =$

$-v_i^F$, and the orientations, $\hat{p}_i^B = (\cos \theta_{i+1}, \sin \theta_{i+1})$, $i = 1 \dots d$. Note that backward orientations are shifted by one frames, compared to the forward one. Trajectories for $-1/2$ defects are computed similarly, taking into account the three-fold symmetry as described above.

See below for the estimation method for Kullback-Leibler divergence.

Quantifying irreversibility in defect pairs

First, the data for each defect trajectory or defect-pair was reduced to include only a few relative angles, as described in the results section. Looking only at the first (last) D samples right after (before) a creation (annihilation) event, each event corresponds to an effective vector \mathbf{f}_i . For example, looking only at the relative angle between the $+^{1/2}$ and $-^{1/2}$ defects, each creation event is reduced to a D -dimensional vector $\mathbf{f}_i = (\Theta_1 \dots \Theta_D)$, where Θ_1 is the angle closest to creation. The time-reversed trajectory is simply $\mathbf{b}_i = (\Theta_D \dots \Theta_1)$.

The informatic entropy production is the Kullback-Leibler divergence between the distribution of forward observations \mathbf{f}_i and backward ones \mathbf{b}_i . Hence, our experimental data provides us with samples from both spaces. In order to evaluate EP, we look at the sequence of projections and find the KLD between the density of forward and backward trajectories. In backward trajectories, the sequence of positions is inverted, and the velocity changes sign. Defect angles do not change; hence the projection also changes sign. Cutting trajectories into 2-frame snippets, we obtain a coarse-grained picture, which is a lower bound of the actual EP.

Finally, cross entropy between the annihilation and creation is defined as the sum of $\text{KLD}(\text{forward creation} \parallel \text{backward annihilation}) + \text{KLD}(\text{forward annihilation} \parallel \text{backward creation})$. See below for the estimation method.

Estimation of Kullback-Leibler divergence

Let F and B denote continuous distributions over \mathbb{R}^D such that F is absolutely continuous with respect to B . The densities are denoted $f(x)$ and $b(x)$, respectively. We would like to estimate the Kullback-Leibler divergence of F with respect to B ,

$$D_{\text{KL}}(F \parallel B) = \int_{\mathbb{R}^D} f(x) \ln \frac{f(x)}{b(x)} dx, \quad (1)$$

using independent samples $\mathbf{f}_1 \dots \mathbf{f}_N$ and $\mathbf{b}_1 \dots \mathbf{b}_M$, taken from F and B respectively. Throughout, we take $0 \ln 0/0 = 0$.

Here, the divergence is estimated using the k -nearest neighbors (k NN) suggested by Wang et al [58]. The main idea is as follows. We note that the D_{KL} can be written

as an average,

$$D_{\text{KL}}(F||B) = \left\langle \ln \frac{f(X)}{b(X)} \right\rangle, \quad (2)$$

where X denotes a random variable with distribution F . Let $k \ll N, M$. Locally, around a sample point \mathbf{f}_i , the density $f(x)$ can be approximated as

$$f(\mathbf{f}_i) \simeq \frac{k}{N-1} \frac{1}{V_D \rho_k^D(i)}, \quad (3)$$

where V_D is the volume of the unit ball in \mathbb{R}^D and $\rho_k(i)$ is the (Euclidean) distance from position \mathbf{f}_i of point i , to the k 's NN out of $\mathbf{f}_1 \dots \mathbf{f}_N$ (not counting i itself, hence $N-1$). Similarly, the density $b(x)$ around a sample point i , can be approximated as

$$b(\mathbf{f}_i) \simeq \frac{k}{M} \frac{1}{V_D \nu_k^D(i)}, \quad (4)$$

$\nu_k(i)$ is the distance from \mathbf{f}_i to the k 's NN out of $\mathbf{b}_1 \dots \mathbf{b}_M$. Substituting into (2) yields,

$$D_{\text{KL}}(F||B) \simeq \frac{D}{N} \sum_{i=1}^N \frac{\nu_k(i)}{\rho_k(i)} + \ln \frac{M}{N-1}. \quad (5)$$

See [58] for a proof (5) is a consistent estimator for $D_{\text{KL}}(F||B)$.

To estimate the statistical error, we recall that the divergence is an average quantity. Accordingly (see also [59] for similar considerations for estimation of entropy), we take the standard error to be

$$\sigma_{\text{KL}}(F||B) = \frac{1}{\sqrt{N}} \text{std} \left[\ln \frac{f(X)}{b(X)} \right], \quad (6)$$

where std denotes the standard deviation. Once again, approximating the densities using kNN yield an estimator for the standard error [59].

The parameter k , setting the number of neighbors, should be taken to be proportional to \sqrt{N} [59]. Estimates reported for single-defects, single cells and the nematic/flow fields used $k = \sqrt{N}$. EP of defect pairs use only the orientation of defect, which are discretized. As a result, angles are not unique and the distance between neighbors may be zero. To this end, we use a larger value of $k = 2\sqrt{N}$.

Combining polar and nematic vector fields

The cells are long, thin objects with a shape that is broadly identical under π rotation of the director. At high density, they form a thin layer with local orientational order. To describe the average orientation local of the we cells we introduce the director field \hat{n} defined as:

$$\hat{n} = [\cos(\psi), \sin(\psi)] \quad (7)$$

where ψ is the average orientation of the cells at a point in space.

Most observations on the cells are compatible with the typical nematic active stress:

$$\sigma_{ij} \sim (\hat{n}_i \hat{n}_j - \delta_{ij}/2) \quad (8)$$

This is the lowest order active term consistent with conservation of momentum and nematic symmetry.

However, the cells here are able to self-propel, exchanging momentum with the substrate leading to an additional active body force on the material given. We introduce the second director field \hat{p} , which describes the self-propulsion direction of the cells. This can lead to a body force of the form:

$$\underline{f} \sim \hat{p} \quad (9)$$

The cells are elongated in shape and self-propel along their long axis, meaning that \hat{p} and \hat{n} must be either parallel or anti-parallel, i.e. $(\hat{p} \cdot \hat{n})^2 = 1$.

We introduce a polar director angle θ such that:

$$\hat{p} = [\cos(\theta), \sin(\theta)] \quad (10)$$

Which implies that either $\theta = \psi$ or $\theta = \psi + \pi$.

Field around a topological defect

Topological defects within the nematic field are characterized by a half integer winding number $k = \pm 1/2$. The director field at a polar angle ϕ around a topological defect is given by:

$$\psi = k\phi + \psi_0 \quad (11)$$

where we have introduced a phase ψ_0 which corresponds to a global rotation of the defect by an angle of $\frac{\psi_0}{1-k}$. Note, here we will adopt the convention that $\phi \in [-\pi, \pi]$ for convenience and $\psi_0 = 0$ which fixes the orientation of the defect relative to the frame of reference. Examples of these defects are given in Extended Data Fig. 3.

A half integer winding number is incompatible with the polar field \hat{p} , and necessitates the introduction of a discontinuous jump in the polar director angle, θ . This is the grain boundary over which \hat{p} goes through a π rotation which begins and ends at a topological defect. We introduce the grain boundary as follows

$$\theta = k\phi + \psi_0 + \pi * (H(\phi - \phi_g) + m) \quad (12)$$

$m \in \{0, 1\}$ corresponds to a global rotation of \hat{p} by π and captures the additional symmetry of the polar field relative to a nematic field. The grain boundary is introduced with a Heaviside step function given by:

$$H(\phi - \phi_g) = \begin{cases} 0, & \phi < \phi_g \\ 1, & \phi > \phi_g \end{cases} \quad (13)$$

ϕ_g describes the polar angle at which the grain boundary approaches the core of the topological defect. Without loss of generality, we constrain $\phi_g \in (-\pi, \pi]$. The grain boundary and resulting polar field are shown in Extended Data Fig. 3.

Total force on a topological defect core due to polar forcing

We now calculate the total additional force on the defect core due to polar forcing by integrating the polar force azimuthally around the core of the defect. Without loss of generality we set $\psi_0 = 0$, which fixes the orientation of the defect. This results in the tail of the $+^{1/2}$ defect, or one of the legs of the $-^{1/2}$ defect, pointing in the $\phi = 0$ direction, which we set as the $+\hat{x}$ direction.

The grain boundary breaks the mirror symmetry of a $+^{1/2}$ defect if it is introduced at any angle other than that opposite to the tail of the defect. Thus in most cases, the $+^{1/2}$ defect becomes chiral.

The total body force around the core of the defect with charge k is given by.

$$\underline{F} = \oint \underline{f}(\phi) d\phi \quad (14)$$

$$\sim \oint \hat{\underline{p}}(\phi) d\phi \quad (15)$$

$$(16)$$

It is convenient to evaluate this integral piecewise to find the solution:

$$\begin{aligned} \underline{F} &\sim \int_{-\pi}^{\phi_g} \hat{\underline{p}}(\phi) d\phi + \int_{\phi_g}^{\pi} \hat{\underline{p}}(\phi) d\phi \\ &= \int_{-\pi}^{\phi_g} [\cos(k\phi + m\pi), \sin(k\phi + m\pi)] d\phi + \\ &\quad + \int_{\phi_g}^{\pi} [\cos(k\phi + (m+1)\pi), \sin(k\phi + (m+1)\pi)] d\phi \\ &= \left[\frac{[\sin(k\phi + m\pi), -\cos(k\phi + m\pi)]}{k} \right]_{-\pi}^{\phi_g} + \\ &\quad + \left[\frac{[\sin(k\phi + (m+1)\pi), -\cos(k\phi + (m+1)\pi)]}{k} \right]_{\phi_g}^{\pi} \\ &= \frac{2}{k} [\sin(k\phi_g + m\pi), -\cos(k\phi_g + m\pi)] \\ &= \frac{2}{k} [\cos(k\phi_g + (m-0.5)\pi), \sin(k\phi_g + (m-0.5)\pi)] \end{aligned}$$

This force is shown as the large red arrow in Extended Data Fig. 3. Some important things to note here.

First, there is a net translational force on both $\pm^{1/2}$ defects, meaning that we expect both defects to self-propel. This is in addition to the self-propulsion force already present for $+^{1/2}$ defects due to the nematic active stress.

If $\phi_g = 0$, as is the case immediately after creation, the additional force is perfectly perpendicular to the symmetry axis of the defect. This would imply a self-propulsion perpendicular to the tail for $+^{1/2}$ defects (or a leg for $-^{1/2}$ defects).

The additional force on the defects breaks chiral symmetry provided it does not align with a mirror symmetry axis of the defect. The mirror symmetry axes of the defect are given by $\phi_s = n\pi/2(k-1)$, $n \in \mathbb{Z}$. In addition, m rotates the force by π meaning it changes the sign of the additional force. This switches the chirality of the effect. As mentioned in the main text, m arises from a spontaneously broken symmetry.

Total torque on a topological defect core due to polar forcing

We can assess the active torsional force around a defect caused by the polar active force by azimuthally integrating the azimuthal component of the polar force. This is given by:

$$\tau = \oint \underline{f} \cdot \underline{dl} \quad (17)$$

This integration is performed on a circle around the defect and \underline{dl} is tangent to that circle. Thus we can write:

$$\tau \sim \int_{-\pi}^{\pi} \hat{\underline{p}} \cdot [-\sin(\phi), \cos(\phi)] d\phi \quad (18)$$

We can simplify this with angle addition formula to obtain:

$$\tau \sim \int_{-\pi}^{\pi} \sin(\theta - \phi) d\phi \quad (19)$$

$$= \int_{-\pi}^{\pi} \sin((k-1)\phi + \pi * (H(\phi - \phi_g) + m)) d\phi \quad (20)$$

$$= \left[\frac{-\cos((k-1)\phi + m\pi)}{k-1} \right]_{-\pi}^{\phi_g} + \quad (21)$$

$$+ \left[\frac{-\cos((k-1)\phi + (m+1)\pi)}{k-1} \right]_{\phi_g}^{\pi} \quad (22)$$

$$= \frac{1}{k-1} [2 \cos((k-1)\phi_g + (m+1)\pi) + \cos(m\pi) - \cos((2k+m-1)\pi)] \quad (23)$$

$$= \frac{2}{1-k} \cos((k-1)\phi_g + m\pi) \quad (25)$$

This torque is shown as the large green arrow in Extended Data Fig. 3.

Some things to note here:

First, the sign of the torque depends on m , thus is selected by a spontaneous symmetry break.

Second, the magnitude of the torque depends on the orientation of the grain boundary. The torque disappears when $(k-1)\phi_g + m\pi = (n+0.5)\pi$, $n \in \mathbb{Z}$. This is

equivalent to when the net additional net force aligns with an axis of mirror symmetry.

Third, the magnitude of the torque additionally depends on k , with $+^1/2$ defects experiencing three times

more torque on their core than $-^1/2$ defects.

IV. SUPPLEMENTARY MATERIAL

-
- [1] T. Sanchez, D. T. Chen, S. J. DeCamp, M. Heymann and Z. Dogic, *Nature*, 2012, **491**, 431–434.
- [2] P. Guillamat, Ž. Kos, J. Hardouin, J. Ignés-Mullol, M. Ravnik and F. Sagués, *Science advances*, 2018, **4**, eaao1470.
- [3] A. J. Tan, E. Roberts, S. A. Smith, U. A. Olvera, J. Arteaga, S. Fortini, K. A. Mitchell and L. S. Hirst, *Nature Physics*, 2019, **15**, 1033–1039.
- [4] N. Kumar, R. Zhang, J. J. De Pablo and M. L. Gardel, *Science advances*, 2018, **4**, eaat7779.
- [5] A. Sokolov, M. M. Apodaca, B. A. Grzybowski and I. S. Aranson, *Proceedings of the National Academy of Sciences*, 2010, **107**, 969–974.
- [6] C. Beta, L. Edelstein-Keshet, N. Gov and A. Yochelis, *Elife*, 2023, **12**, e87181.
- [7] M. C. Marchetti, J.-F. Joanny, S. Ramaswamy, T. B. Liverpool, J. Prost, M. Rao and R. A. Simha, *Reviews of modern physics*, 2013, **85**, 1143–1189.
- [8] L. Giomi, *Physical Review X*, 2015, **5**, 031003.
- [9] S. Zhou, A. Sokolov, O. D. Lavrentovich and I. S. Aranson, *Biophysical Journal*, 2014, **106**, 420a.
- [10] M. Serra, L. Lemma, L. Giomi, Z. Dogic and L. Mahadevan, *Nature Physics*, 2023, **19**, 1355–1361.
- [11] P. Guillamat Bassedas, J. Ignés i Mullol and F. Sagués i Mestre, *Nature Communications*, 2017, vol. 8, num. 564, 2017.
- [12] H. Li, X.-q. Shi, M. Huang, X. Chen, M. Xiao, C. Liu, H. Chaté and H. Zhang, *Proceedings of the National Academy of Sciences*, 2019, **116**, 777–785.
- [13] V. Yashunsky, D. J. Pearce, G. Ariel and A. Be'er, *Soft Matter*, 2024, **20**, 4237–4245.
- [14] T. Shimaya and K. A. Takeuchi, *PNAS nexus*, 2022, **1**, pgac269.
- [15] K. Copenhagen, R. Alert, N. S. Wingreen and J. W. Shaevitz, *Nature Physics*, 2021, **17**, 211–215.
- [16] M. M. Genkin, A. Sokolov, O. D. Lavrentovich and I. S. Aranson, *Physical Review X*, 2017, **7**, 011029.
- [17] T. B. Saw, A. Doostmohammadi, V. Nier, L. Kocgozlu, S. Thampi, Y. Toyama, P. Marcq, C. T. Lim, J. M. Yeomans and B. Ladoux, *Nature*, 2017, **544**, 212–216.
- [18] L. Balasubramaniam, A. Doostmohammadi, T. B. Saw, G. H. N. S. Narayana, R. Mueller, T. Dang, M. Thomas, S. Gupta, S. Sonam, A. S. Yap et al., *Nature materials*, 2021, **20**, 1156–1166.
- [19] C. Blanch-Mercader, V. Yashunsky, S. Garcia, G. Duclos, L. Giomi and P. Silberzan, *Physical review letters*, 2018, **120**, 208101.
- [20] A. Be'er and G. Ariel, *Movement ecology*, 2019, **7**, 1–17.
- [21] I. S. Aranson, *Reports on Progress in Physics*, 2022, **85**, 076601.
- [22] A. Doostmohammadi and B. Ladoux, *Trends in cell biology*, 2022, **32**, 140–150.
- [23] G. Duclos, C. Erlenkämper, J.-F. Joanny and P. Silberzan, *Nature Physics*, 2017, **13**, 58–62.
- [24] K. Kawaguchi, R. Kageyama and M. Sano, *Nature*, 2017, **545**, 327–331.
- [25] R. Ienaga, K. Beppu and Y. T. Maeda, *Soft Matter*, 2023, **19**, 5016–5028.
- [26] V. Venkatesh, N. de Graaf Sousa and A. Doostmohammadi, *Journal of Physics A: Mathematical and Theoretical*, 2025.
- [27] X.-q. Shi and H. Chaté, *arXiv preprint arXiv:1807.00294*, 2018.
- [28] R. Großmann, I. S. Aranson and F. Peruani, *Nature communications*, 2020, **11**, 5365.
- [29] L. C. Head, C. Doré, R. R. Keogh, L. Bonn, G. Negro, D. Marenduzzo, A. Doostmohammadi, K. Thijssen, T. López-León and T. N. Shendruk, *Nature Physics*, 2024, **20**, 492–500.
- [30] L. Huber, R. Suzuki, T. Krüger, E. Frey and A. Bausch, *Science*, 2018, **361**, 255–258.
- [31] O. J. Meacock, A. Doostmohammadi, K. R. Foster, J. M. Yeomans and W. M. Durham, *Nature Physics*, 2021, **17**, 205–210.
- [32] Y. Maroudas-Sacks, L. Garion, L. Shani-Zerbib, A. Livshits, E. Braun and K. Keren, *Nature Physics*, 2021, **17**, 251–259.
- [33] A. Amiri, R. Mueller and A. Doostmohammadi, *Journal of Physics A: Mathematical and Theoretical*, 2022, **55**, 094002.
- [34] M. Lacroix, B. Smeets, C. Blanch-Mercader, S. Bell, C. Giuglaris, H.-Y. Chen, J. Prost and P. Silberzan, *Nature Physics*, 2024, **20**, 1324–1331.
- [35] S. P. Thampi, R. Golestanian and J. M. Yeomans, *Philosophical Transactions of the Royal Society A: Mathematical, Physical and Engineering Sciences*, 2014, **372**, 20130366.
- [36] S. Shankar, S. Ramaswamy, M. C. Marchetti and M. J. Bowick, *Physical review letters*, 2018, **121**, 108002.
- [37] A. Patelli, I. Djafer-Cherif, I. S. Aranson, E. Bertin and H. Chaté, *Physical review letters*, 2019, **123**, 258001.
- [38] L. Bonn, A. Ardaševa, R. Mueller, T. N. Shendruk and A. Doostmohammadi, *Physical Review E*, 2022, **106**, 044706.
- [39] D. Pearce, J. Nambisan, P. Ellis, A. Fernandez-Nieves and L. Giomi, *Physical Review Letters*, 2021, **127**, 197801.
- [40] S. Shankar, A. Souslov, M. J. Bowick, M. C. Marchetti and V. Vitelli, *Nature Reviews Physics*, 2022, **4**, 380–398.
- [41] D. J. Pearce and K. Kruse, *Soft Matter*, 2021, **17**, 7408–7417.
- [42] X. Tang and J. V. Selinger, *Soft matter*, 2017, **13**, 5481–5490.
- [43] A. J. Vromans and L. Giomi, *Soft matter*, 2016, **12**, 6490–6495.
- [44] A. Fernandez-Nieves, A. De La Cotte, D. Pearce, J. Nambisan, A. Levy and L. Giomi, *available at Research Square*, 2024.

TABLE III: Entropy production (EP) estimation - control. Top: EP for trajectories of individual bacteria and cells. Bottom: EP for the nematic and flow fields at random positions. Values show the estimate \pm the standard error. Since this is a lower bound, a value that is statistically larger than zero implies non reversible dynamics. See the methods section for details.

	Bacteria	Cells
EP individual trajectories	-0.004 ± 0.004	0.003 ± 0.0002
EP nematic+flow	0.0008 ± 0.001	0.0008 ± 0.001

- [45] V. Yashunsky, D. Pearce, C. Blanch-Mercader, F. Ascione, P. Silberzan and L. Giomi, *Physical Review X*, 2022, **12**, 041017.
- [46] B. Martínez-Prat, R. Alert, F. Meng, J. Ignés-Mullol, J.-F. Joanny, J. Casademunt, R. Golestanian and F. Sagués, *Physical Review X*, 2021, **11**, 031065.
- [47] A. Ardaševa, I. Vélez-Cerón, M. C. Pedersen, J. Ignés-Mullol, F. Sagués and A. Doostmohammadi, *Physical Review Letters*, 2025, **134**, 088301.
- [48] B. Palmer, S. Chen, P. Govan, W. Yan and T. Gao, *Soft Matter*, 2022, **18**, 1013–1018.
- [49] K. Prathyusha, S. Henkes and R. Sknepnek, *Physical Review E*, 2018, **97**, 022606.
- [50] A. Joshi, E. Putzig, A. Baskaran and M. F. Hagan, *Soft Matter*, 2019, **15**, 94–101.
- [51] U. Seifert, *Reports on progress in physics*, 2012, **75**, 126001.
- [52] É. Fodor, R. L. Jack and M. E. Cates, *Annual Review of Condensed Matter Physics*, 2022, **13**, 215–238.
- [53] S. Ro, B. Guo, A. Shih, T. V. Phan, R. H. Austin, D. Levine, P. M. Chaikin and S. Martiniani, *Physical review letters*, 2022, **129**, 220601.
- [54] M. J. Bowick, N. Fakhri, M. C. Marchetti and S. Ramaswamy, *Physical Review X*, 2022, **12**, 010501.
- [55] G. Pisegna, S. Saha and R. Golestanian, *Proceedings of the National Academy of Sciences*, 2024, **121**, e2407705121.
- [56] B. H. Andersen, F. M. Safara, V. Grudtsyna, O. J. Meacock, S. G. Andersen, W. M. Durham, N. A. Araujo and A. Doostmohammadi, *Nature Physics*, 2025, 1–6.
- [57] K. Vaidžiulytė, A.-S. Macé, A. Battistella, W. Beng, K. Schauer and M. Coppey, *Elife*, 2022, **11**, e69229.
- [58] Q. Wang, S. R. Kulkarni and S. Verdú, *IEEE Transactions on Information Theory*, 2009, **55**, 2392–2405.
- [59] J. Beirlant, E. J. Dudewicz, L. Györfi, E. C. Van der Meulen *et al.*, *International Journal of Mathematical and Statistical Sciences*, 1997, **6**, 17–39.

FUNDING

The research was supported by The Israel Science Foundation (grants no. 838/23, 2044/23, 382/23 and 161/24). DJGP and DC acknowledge funding from the Swiss National Science Foundation under starting grant TMSGI2 211367.

AUTHOR CONTRIBUTIONS

A.B., G.A. and V.Y. designed research, A.B. and V.Y. performed the experiments, D.C., and D.J.G.P. did the theoretical part, A.B., E.D.N., D.C., D.J.G.P., G.A. and V.Y. analysed data, and A.B., E.D.N., D.C., D.J.G.P., G.A. and V.Y. wrote the paper.

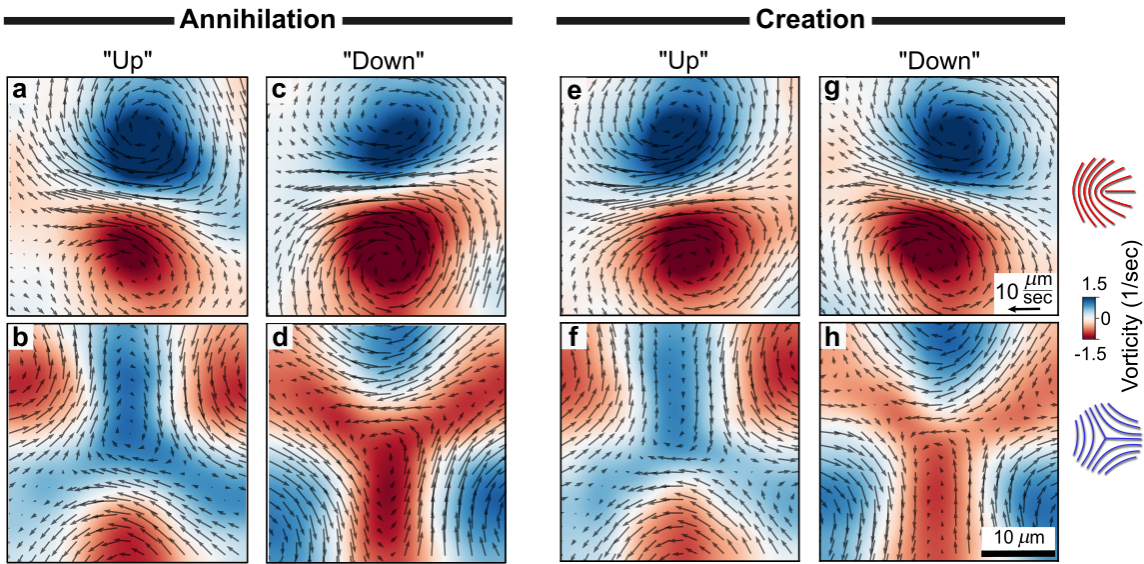
COMPETING INTERESTS

There are no competing interests to declare.

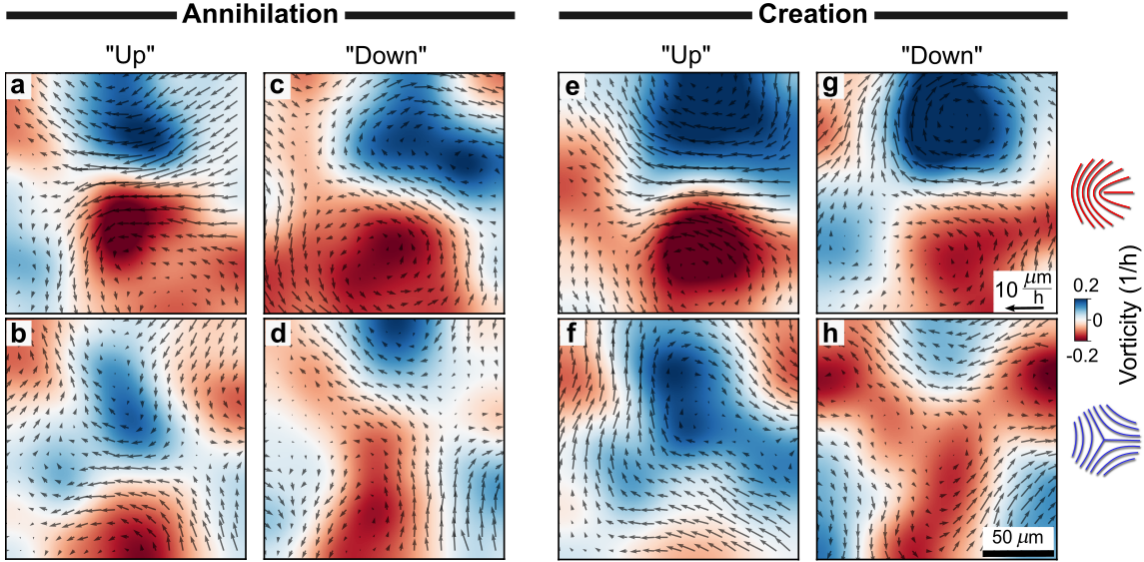
DATA AND MATERIALS AVAILABILITY

Original data will be available by the authors upon reasonable request. The code for the analyses of the experimental data can be accessed via GitLab at <https://github.com/viciya/nematics>.

EXTENDED DATA

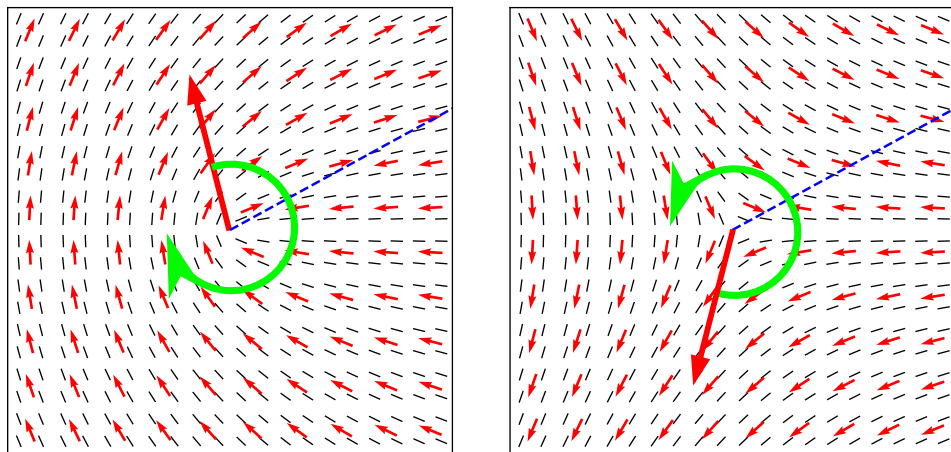


Extended Data Fig. 1: Ensemble-averaged flow fields near $\pm\frac{1}{2}$ defect-pairs in bacterial swarm.
 Average velocity fields (black arrows) and vorticity distributions (heatmap) around defects. Flow fields around paired $+\frac{1}{2}$ and $-\frac{1}{2}$ defects, averaged separately for the “up” (a, b, e, f) and “down” (c, d, g, h) configurations for annihilation (a, b, c, d) and creation events (e, f, g, h).



Extended Data Fig. 2: Ensemble-averaged flow fields near $\pm\frac{1}{2}$ defect-pairs in HBEC cell culture.

Average velocity fields (black arrows) and vorticity distributions (heatmap) around defects. Flow fields around paired $+\frac{1}{2}$ and $-\frac{1}{2}$ defects, averaged separately for the “up” (a, b, e, f) and “down” (c, d, g, h) configurations for annihilation (a, b, c, d) and creation events (e, f, g, h).



Extended Data Fig. 3: Polar fields around a $+\frac{1}{2}$ and $-\frac{1}{2}$ defect. Half integer defects are shown in the nematic field (black lines). The polar field (small red arrows) around a half integer defect necessitates the existence of a grain boundary (blue dashed line) over which the polar field switches direction. At the core of the defect, the polar field has a net orientation (large red arrow) and net curl (green arrow). This corresponds to an additional force and torque on the defect core, respectively. The left shows a $k = 0.5$ charge defect and the right shows a $k = -0.5$ defect. Both defects are presented with zero phase, $\psi_0 = 0$. The grain boundary in both cases is at $\phi_g = 0.5$ and $m = 1$.